Space–charge theory applied to the grain boundary impedance of proton conducting $BaZr_{0.9}Y_{0.1}O_{3-\delta}$

Christian Kjølseth [a], Harald Fjeld [a], Øystein Prytz [b], Paul Inge Dahl [c,1], Claude Estournès [d], Reidar Haugsrud [a], Truls Norby [a,*]

[a] Centre for Materials Science and Nanotechnology, Department of Chemistry, University of Oslo, FERMiO, Gaustadalléen 21, NO-0349 Oslo, Norway
[b] Department of Physics, University of Oslo, POB 1048 Blindern, NO-0316, Oslo, Norway
[c] Department of Materials Technology, Norwegian University of Science and Technology, NO-7491 Trondheim, Norway
[d] CNRS, Institut Carnot Cirimat and Plateforme Nationale de Frittage Flash (PNF2-CNRS), F-31062 Toulouse Cedex 09, France

Keywords:
$BaZrO_3$
$BaZr_{0.9}Y_{0.1}O_{3-\delta}$
Proton conductivity
Grain boundary resistance
Impedance spectroscopy
Space–charge layer

A B S T R A C T

The specific grain interior and grain boundary conductivities, obtained from impedance spectroscopy and the brick layer model, are reported for $BaZr_{0.9}Y_{0.1}O_{3-\delta}$ as a function of p_{O_2} and temperature. p_{O_2}-dependencies were indicative of dominating ionic and p-type electronic conduction for the grain interior under reducing and oxidizing conditions, respectively, while the grain boundaries showed an additional n-type electronic contribution under reducing conditions. Transmission electron microscopy revealed enrichment of Y in the grain boundary region. These findings indicate the existence of space–charge layers in the grain boundaries. A grain boundary core–space–charge layer model is therefore applied to interpret the data. Using a Mott–Schottky approximation, a Schottky barrier height of 0.5–0.6 V and an effective grain boundary width of 8–10 nm (=2× space–charge layer thickness) is obtained at 250 °C in wet oxygen. Finite-element modelling of the complex impedance over a grain boundary with a space–charge layer depletion of protons yields a distorted semicircle as observed in the impedance spectra.

1. Introduction

High electrical resistance in the grain boundaries is observed for several types of conductors such as the oxide ion conducting Y-doped ZrO_2 (YSZ) [1] and Gd-doped CeO_2 (CGO) [2], the mixed electron-oxide ion conducting Fe-doped $SrTiO_3$ [3] and the proton conducting Gd-doped $BaCeO_3$ [4], Y-doped $BaZrO_3$ [5,6] and Ca-doped $LaNbO_4$ [7]. $BaZr_{0.9}Y_{0.1}O_{3-\delta}$ has one of the highest reported grain interior proton conductivities of the perovskite oxides, $6.5 \cdot 10^{-3}$ S cm^{-1} in wet air at 600 °C [5] and a better chemical and mechanical stability than the corresponding barium and strontium cerates [8] under conditions with acidic gas impurities, e.g. CO_2. Possible applications as electrolyte in fuel cells and steam electrolysers may however be limited because of dominating grain boundary resistance.

The high grain boundary resistance in ionic conductors has commonly been attributed to highly resistive or blocking impurity phases at the grain boundaries. However, studies on high-purity materials have shown that there also exists an intrinsic grain boundary resistance in high-purity materials. Both extrinsic and intrinsic grain boundary resistances have been thoroughly investigated for oxide ion conductors [9–16], but for proton conductors little has been reported so far, see for instance [17,18]. In the present work we study the grain boundary resistance of $BaZr_{0.9}Y_{0.1}O_{3-\delta}$, applying models for the intrinsic grain boundary properties used for oxide ion conductors [1,14,19,20] using $BaZr_{0.9}Y_{0.1}O_{3-\delta}$ samples sintered by hot pressing and spark plasma sintering.

We have studied the electrical properties of the grain interior and grain boundaries with impedance spectroscopy in the temperature interval 500–150 °C. Furthermore, the electrical properties were investigated as a function of oxygen partial pressure, which gives information of the dominating charge carrier using defect chemical analysis. Below 350 °C the concentration of protons can be considered "frozen-in" [5] and at these temperatures, qualitative partial pressure dependencies were obtained by equilibration in each atmosphere at 700 °C before measuring at the lower temperature. The brick layer model (BLM), explained in detail by Haile et al. [4], is applied, from which the effective grain boundary width and specific grain boundary conductivity can be estimated. The BLM assumes cubic grains with grain boundaries parallel and serial to adjacent grains. The validity and limitations of the BLM have been elaborated by Fleig et al. [21,22], treating effects such as constricted current paths from imperfect contacts between the grains and influence of inhomogeneous microstructures on the analysis of grain boundary impedances. The

Corresponding author. Tel.: +47 22840654; fax: +47 22840651.
E-mail address: trulsn@kjemi.uio.no (T. Norby).
[1] Present affiliation: SINTEF Materials and Chemistry, Department of Energy Conversion and Materials, Forskningsveien 1, NO-0314 Oslo, Norway.

present work discusses the influence of such deviations on the complex impedance.

Investigations of the intrinsic grain boundary conductivity of nominally impurity-free oxide ion conductors have given indications on the existence of space–charge layers which govern the grain boundary resistance. In the present work we apply similar approaches to evaluate the role and properties of space–charge layers in the grain boundaries of proton conducting ceramics, with $BaZr_{0.9}Y_{0.1}O_{3-\delta}$ as the experimental example.

2. Grain boundary core–space–charge layer model

The intrinsic grain boundary properties of the oxide ion conductors Y-doped ZrO_2 (YSZ) and Gd-doped CeO_2 (CGO) have been successfully interpreted by a grain boundary core–space–charge layer model [14,23–26]. A general solution of the space–charge theory has been given by Kim et al. [25] in which the case for singly charged carriers such as protons is included. The model describes a grain boundary in electrical terms as consisting of a core with two adjacent space–charge layers as depicted in Fig. 1. For these oxide ion conductors, it has been observed experimentally that divalent and trivalent solutes are enriched in the grain boundary zone and not only in the grain boundary core, while there is no enrichment of tetra- and pentavalent solutes. This indicates a positive grain boundary core with adjacent negative space–charge layers [27], in which the enrichment of the lower-valent solutes makes up part of the net negative charge of the space–charge layer. The charge of the core was concluded to be an inherent materials property. Likewise, segregation of acceptor solutes in the grain boundaries has been observed for proton conductors in $BaZr_{0.85}Y_{0.15}O_{3-\delta}$ [28], which as for the oxide ion conductors indicates that the grain boundary core is positive and the space–charge layers negative.

In the following we will derive the grain boundary core–space charge model for the case of proton conductors. The important factor governing the defect concentration profile in the space–charge layer is the electrochemical potential of the defect through the grain boundary and grain interior. First we define the intercept between the grain boundary core and the space–charge layer, shown in Fig. 1, as position $x=0$ and the grain interior as $x=\infty$. The electrochemical potential of a mobile proton as a function of distance x, is then ideally (assuming unity activity coefficient) given by

$$\eta_{H^+}(x) = \mu^0_{H^+} + k_B T \ln c_{H^+}(x) + e\varphi(x) \tag{1}$$

where $\mu^0_{H^+}$ is the standard chemical potential of protons, $c_{H^+}(x)$ the proton concentration, $\varphi(x)$ the electrostatic potential, and e, k_B and T have their usual meanings. In the grain interior, the electrochemical potential of the proton is then given by

$$\eta_{H^+}(\infty) = \mu^0_{H^+} + k_B T \ln c_{H^+}(\infty) + e\varphi(\infty). \tag{2}$$

At equilibrium, where $\eta_{H^+}(x)=\eta_{H^+}(\infty)$, the difference in electrostatic potential relative to grain interior, $\Delta\varphi(x)=\varphi(x)-\varphi(\infty)$, is then

$$\Delta\varphi(x) = \frac{k_B T}{e} \ln \frac{c_{H^+}(\infty)}{c_{H^+}(x)} \tag{3}$$

and, consequently,

$$\frac{c_{H^+}(x)}{c_{H^+}(\infty)} = \exp\left(-\frac{e\Delta\varphi(x)}{k_B T}\right). \tag{4}$$

From the Poisson equation we have

$$\frac{d^2\Delta\varphi(x)}{dx^2} = -\frac{1}{\varepsilon} Q(x), \tag{5}$$

where ε is the dielectric constant and $Q(x)$ the net charge density in the space–charge layer.

Onwards we assume that temperatures and water vapour pressures are such that protons are the dominating positive charge compensating defect. If we consider that protons are strongly depleted in the negative space–charge layer, the net charge density, $Q(x)$, can be considered to be governed only by the acceptor concentration:

$$Q(x) = e[c_{H^+}(x) - c_Y(x)] \approx -e c_Y(x). \tag{6}$$

At temperatures where cations can be considered frozen-in, we can apply the Mott–Schottky approximation, which assumes that the

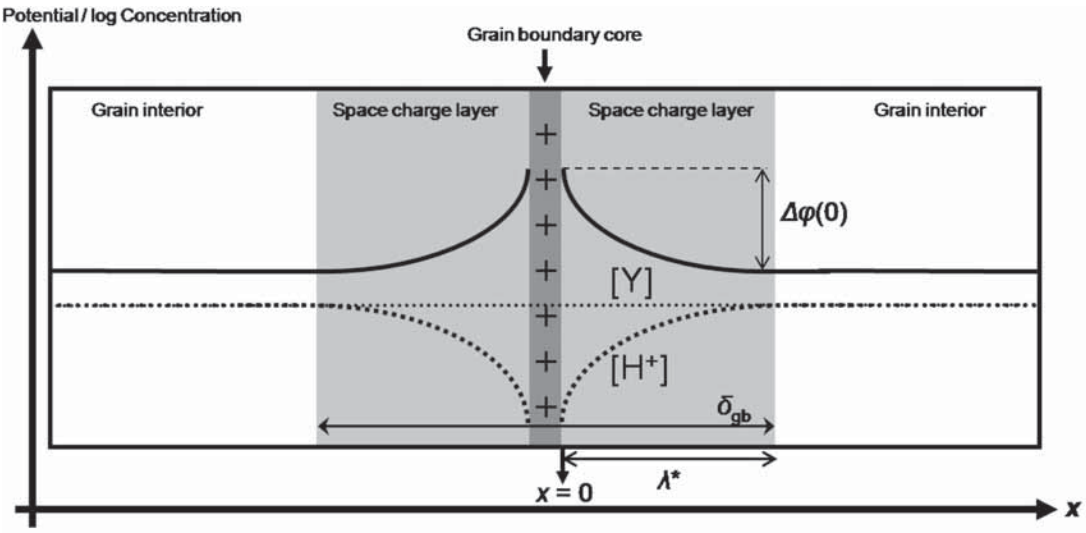

Fig. 1. Schematic grain boundary consisting of a positive core charge compensated by two adjacent space–charge layers. Values of x are defined such that $x=0$ at the interface between the space–charge layer and the grain boundary core, while far into the grain interior $x=\infty$. The dotted lines represent concentration profiles in the space–charge layer for the protons and the acceptor dopant under the Mott–Schottky approximation, while the unbroken line represents the potential profile. The Schottky barrier height potential difference is also indicated.

acceptor concentration is constant up to the grain boundary core, as shown in Fig. 1. At higher temperatures, >1000 °C, where one needs to consider mobile cations, usually a Gouy–Chapman approximation is applied [26]. Only the Mott–Schottky approximation will be considered in the present work. The charge density in the grain boundary region is then given by the concentration of acceptors in the grain interior:

$$Q(x) = -ec_Y(x) = -ec_Y(\infty). \tag{7}$$

Defining the Debye length, L_D as

$$L_D = \left(\frac{k_B T\varepsilon}{2e^2 c_Y(\infty)}\right)^{\frac{1}{2}}, \tag{8}$$

and the effective space–charge layer width, λ^* (Fig. 1) as

$$\lambda^* = 2L_D\left(\frac{e\Delta\varphi(0)}{k_B T}\right)^{\frac{1}{2}} = \left(\frac{2\varepsilon\Delta\varphi(0)}{ec_Y(\infty)}\right)^{\frac{1}{2}}, \tag{9}$$

one can derive an expression for the normalized proton concentration, in the space–charge layer at position x (Fig. 1),

$$\frac{c_{H^+}(x)}{c_{H^+}(\infty)} = \exp\left[-\frac{1}{4}\left(\frac{x-\lambda^*}{L_D}\right)^2\right]. \tag{10}$$

For $x>\lambda^*$, we obviously have $\frac{c_{H^+}(x)}{c_{H^+}(\infty)} = 1$.

The term $\Delta\varphi(0)=\varphi(0)-\varphi(\infty)$ in Eq. (9) is the potential at the intercept between core and space-charge layer, relative to grain interior, and is called the Schottky barrier height. It can be calculated numerically, and in order to approach this we address the ratio of the specific proton conductivity σ_{gi} in the grain interior and the experimentally accessible effective apparent specific proton conductivity σ_{gb} (hereby denoted only as the grain boundary conductivity) in the space–charge regions of the grain boundary. The local proton conductivity in the grain boundary region depends on the distance from the core. The grain boundary conductivity σ_{gb} is therefore the effective property for the entire boundary obtained from integrating the resistance over the thickness of the boundary. Assuming equal mobility of protons in the grain interior and in the grain boundaries, the concentrations in Eq. (4) can be substituted with specific conductivities through the relation $\sigma_{H^+}=ec_{H^+}u_{H^+}$. In order to obtain an expression containing apparent effective grain boundary conductivity over the entire space–charge layer, we first invert Eq. (4) and, in turn, invert the grain boundary conductivity into resistivity:

$$\frac{c_{H^+}(\infty)}{c_{H^+}(x)} = \frac{\sigma_{gi}}{\sigma(x)} = \sigma_{gi}\rho(x) = \exp\left(\frac{e\Delta\varphi(x)}{k_B T}\right) \tag{11}$$

where $\sigma(x)$ and $\rho(x)$ are the proton conductivity and resistivity, respectively, at position x in the space–charge layer. In order to get the apparent effective specific resistivity over the whole space–charge layer thickness we integrate and divide by its thickness to remain with a specific value:

$$\frac{\sigma_{gi}}{\sigma_{gb}} = \sigma_{gi}\rho_{gb} = \frac{1}{\lambda^*}\int_0^{\lambda^*}\exp\left(\frac{e\Delta\varphi(x)}{k_B T}\right)dx. \tag{12}$$

We substitute to get an expression for $\Delta\varphi(x)$ and assume a Mott–Schottky approximation. The further derivation has been shown in [12], and gives the following solution for the case of proton conduction:

$$\frac{\sigma_{gi}}{\sigma_{gb}} \cong \frac{\exp\left(\frac{e\Delta\varphi(0)}{k_B T}\right)}{\frac{2e\Delta\varphi(0)}{k_B T}}. \tag{13}$$

For each of the specific grain interior and grain boundary conductivities we can derive activation energies through $E_A = -\frac{d\ln\sigma T}{d\left(\frac{1}{k_B T}\right)}$. The difference in grain interior and grain boundary activation energy can, through differentiating Eq. (13), be obtained as:

$$\begin{aligned} E_{A,gb}-E_{A,gi} &= (e\Delta\varphi(0)-k_B T)\left[1+\frac{1}{T\Delta\varphi(0)}\frac{d\Delta\varphi(0)}{d\left(\frac{1}{T}\right)}\right] \\ &= (e\Delta\varphi(0)-k_B T)\left[1+\frac{1}{T}\frac{d\ln\Delta\varphi(0)}{d\left(\frac{1}{T}\right)}\right]. \end{aligned} \tag{14}$$

From this we see that the activation energy of the grain boundary conductivity, $E_{A,gb}$, has a contribution from the mobility, i.e., $E_{A,gi}$, and terms that are related to the variation of the concentration of charge carriers in the space–charge layer. These terms contain both the Schottky barrier height itself and the temperature dependence of the Schottky barrier height.

3. Experimental

$BaZr_{0.9}Y_{0.1}O_{3-\delta}$ powder was produced by spray-pyrolysis according to a method described elsewhere [29] with starting materials $Ba(NO_3)_2$, $ZrO(NO_3)_2\cdot xH_2O$ and $Y(NO_3)_3\cdot 6H_2O$. A sample denoted BZY10-HP was sintered by uni-axial hot pressing (HP) at 1650 °C for 1 h under 50 MPa while the sample denoted BZY10-SPS was sintered in a carbon die by spark plasma sintering (SPS), at 1600 °C for 5 min under 100 MPa in vacuum. Both sintering methods yielded relative densities >95%. The very short sintering time enabled by SPS was intended to prevent possible evaporation of BaO. After SPS, the disc was annealed in air at 700 °C for 2 h to remove surface contamination of carbon. Following sintering, the samples were investigated by scanning electron microscopy (FEG-SEM, FEI Quanta 200 with energy dispersive X-ray spectroscopy (EDS, EDAX)) without detecting any sign of impurities. After electrical measurements, the samples were investigated with respect to microstructure and impurities by transmission electron microscopy (TEM, JEOL 2010F with EDS (Noran Vantage DI+)). Neither the grain interior nor grain boundaries showed any sign of impurities, as investigated by means of EDS with a spot size of about 5 nm. However, the EDS analysis revealed a higher concentration of dopant in the grain boundary region compared to the grain interior. Based on TEM characterization, Fig. 2a, the grain size of BZY10-HP was estimated to be 280 nm, while that of BZY10-SPS, Fig. 2b, is bimodal showing grain sizes mostly above ~450 nm and below ~50 nm.

The thicknesses of the samples were 1.85 mm for BZY10-SPS and 2.55 mm for BZY10-HP. Circular Pt electrodes of diameter ~1 cm were attached to each side of the specimens by first painting one layer with Pt ink (Metalor, Pt A3788A) and then adding a Pt net, followed by painting of 3 new layers of ink. To burn off the residual organics from the Pt ink the samples were annealed at 1000 °C for 1 hour. Finally, the samples were mounted in a ProboStat™ (NorECs, Norway) measurement cell for electrical characterization, using 4 wires connected in pairs to the two electrodes.

Electrical characterization was performed in the frequency range 10 MHz to 0.1 Hz, with an oscillation voltage of 0.5 V RMS, using a Novocontrol alpha-A impedance spectrometer with a ZG4 interface. This was done as a function of the oxygen partial pressure, which was controlled by mixing of O_2, Ar, and H_2O for oxidizing conditions, and

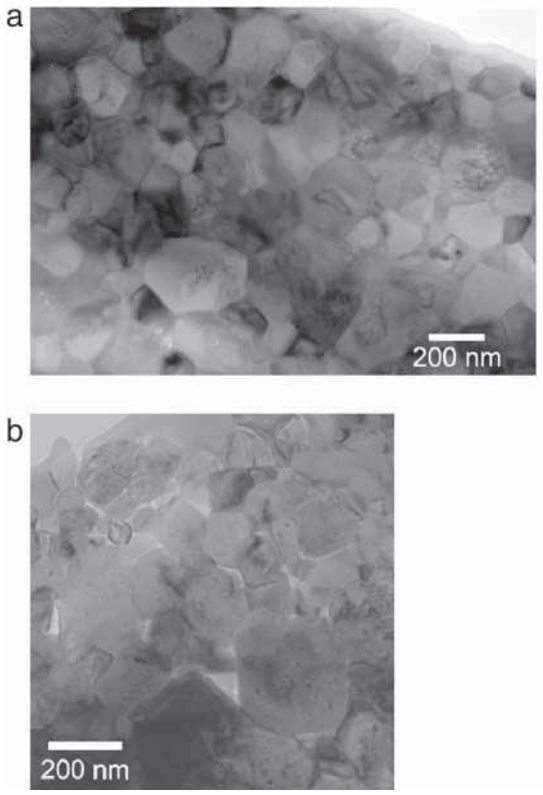

Fig. 2. TEM pictures taken of the microstructure after the electrical measurements a) of BZY10-HP showing a relatively homogeneous grain structure with grain size of ~280 nm, and b) of BZY10-SPS showing a bimodal grain size distribution with grain size of ~450 and ~50 nm.

H_2, Ar, and H_2O for reducing conditions. The water vapour partial pressure in wet gases was fixed by bubbling the gas mixture first through de-ionized water and then through a saturated KBr solution, both at room temperature, yielding 80% relative humidity.

Measurement temperatures were chosen so that impedance spectra showed both the grain interior and grain boundary arcs in a Nyquist plot, as parameters for the grain interior arc is a prerequisite to calculate specific grain boundary conductivities through the BLM [4]. These temperatures were typically between 150 and 300 °C. The impedance spectra were deconvoluted using the "EqC for Windows" software [30] yielding capacitance and conductance parameters for both grain interior and grain boundaries.

The slow kinetics in the temperature regime for measurements lead to "frozen-in" conditions as seen in studies by Bohn and Schober [5,8] in which thermogravimetry of $BaZr_{0.9}Y_{0.1}O_{3-\delta}$ showed that protons are "frozen-in" below ~300 °C and that the material by heating in dry surroundings dehydrates only above ~300–350 °C. In order to have reproducible "frozen-in" concentration of defects, the samples were in our study equilibrated at 700 °C and then cooled at 300°/h to the temperature of measurements (at or below 300 °C). The oxygen partial pressures reported under reducing conditions are the oxygen activities in the H_2+H_2O mixtures at the measurement temperature. This represents a coarse approximation since the defect situation freezes at a higher temperature, but trends in the oxygen activity dependence should still be valid. With respect to hydration, the data should represent a meta-stable (frozen-in) defect situation corresponding to higher temperatures, with a somewhat lower proton concentration than the equilibrium concentration at the actual temperature of the measurement. This "frozen-in" state is mainly a result of the low mobility of oxygen vacancies; as they are considerably slower than protons and limit the chemical diffusion of water needed to reach equilibrium. The difference in mobility also allows us to assume that the material is mainly a proton conductor in the measured temperature range. Finally, it may be noticed that we later on will assume that protons may redistribute in and close to the space–charge layer as a function of temperature in the otherwise "frozen-in" temperature regime.

4. Results and discussion

4.1. Considerations on deconvolution of impedance spectra

Fig. 3 shows Nyquist plots of impedance spectra for (a) BZY10-SPS in wet hydrogen at 250 °C, (b) BZY10-SPS in wet oxygen at 250 °C and (c) BZY10-HP in wet oxygen at 350 °C. For BZY10-SPS under reducing conditions (a) it is possible to see a small grain interior contribution at high frequencies followed by the grain boundary and electrode responses at lower frequencies. Also under oxidizing conditions, a small grain interior contribution is observed (b-I), which is magnified in (b-II) and showing a well-defined semicircle. The same features are observed for BZY10-HP showing the dominant grain boundary semicircle (c-I) and the magnified high frequency part showing the grain interior semicircle (c-II).

All the impedance spectra were deconvoluted after subtraction of a parasitic parallel capacitance, C_{stray}, originating from the measurement setup. The equivalent circuit used for the deconvolution is shown in Fig. 4. The samples' relative dielectric constants, calculated from the grain interior capacitance, are fairly constant with temperature and estimated to ~90 for BZY10-HP and ~70 for BZY10-SPS. The values are somewhat larger than the value 46 reported for BZY20 by Babilo et al. [31]. Due to a distortion in the grain boundary semicircle observed for both specimens, this semicircle was deconvoluted with two (RQ) sub-circuit elements, as shown in Fig. 4, reflecting the possibility of two grain boundary series contributions to the impedance. Distortions in the grain boundary semicircle have been observed also for other polycrystalline materials and suggested to reflect that there are inhomogeneities in terms of microstructure or composition [32]. In BZY10-SPS the non-uniform grain size distribution, as observed in Fig. 2, can be the origin of the distortion, resulting from a frequency dependence of the current paths as shown by a finite-element study by Fleig [33]. In our BZY10-HP sample the microstructure is however more uniform, but we still see a distorted grain boundary semicircle. This therefore suggests that the distortion may have other origins or contributions.

To investigate whether the distortion in fact can originate from the existence of space–charge layers we have simulated (using ZView, Scribner Associates Inc.) an impedance spectrum based on a series of space–charge layer elements through the boundary. The simulated spectrum, presented in Fig. 5, is based on normalized defect concentrations in the space–charge layer profile and on the grain interior conductivity from the BZY10-HP sample at 250 °C in wet O_2. The space–charge layer defect profile will be discussed later on. The impedance of the grain boundary was derived as a series of apparent resistivities (using the BLM backwards) representing finite parts of the space–charge layer profile, R_{gb}, each in parallel with a capacitance, C_{gb}, which was held constant at the value from the deconvoluted experimental spectrum. Finally, the grain interior impedance from the original spectrum was added in the total simulation. As can be seen in Fig. 5 the simulated impedance arc is somewhat smaller than the experimental one, due to the use of a predetermined set of parameters chosen for the modelling, instead of fitting them to the experimental spectrum. These parameters include the doping concentration, the Schottky barrier height and the relative dielectric constant. A spectrum simulated with an effective dopant concentration of 7.5% fits better to the experimental spectrum, see Fig. 5. A somewhat lower dopant concentration has indeed been indicated by EDS analyses. Regardless of the exact magnitude of the arcs, the simulated spectra are seen to exhibit a clear distortion similar to the experimental

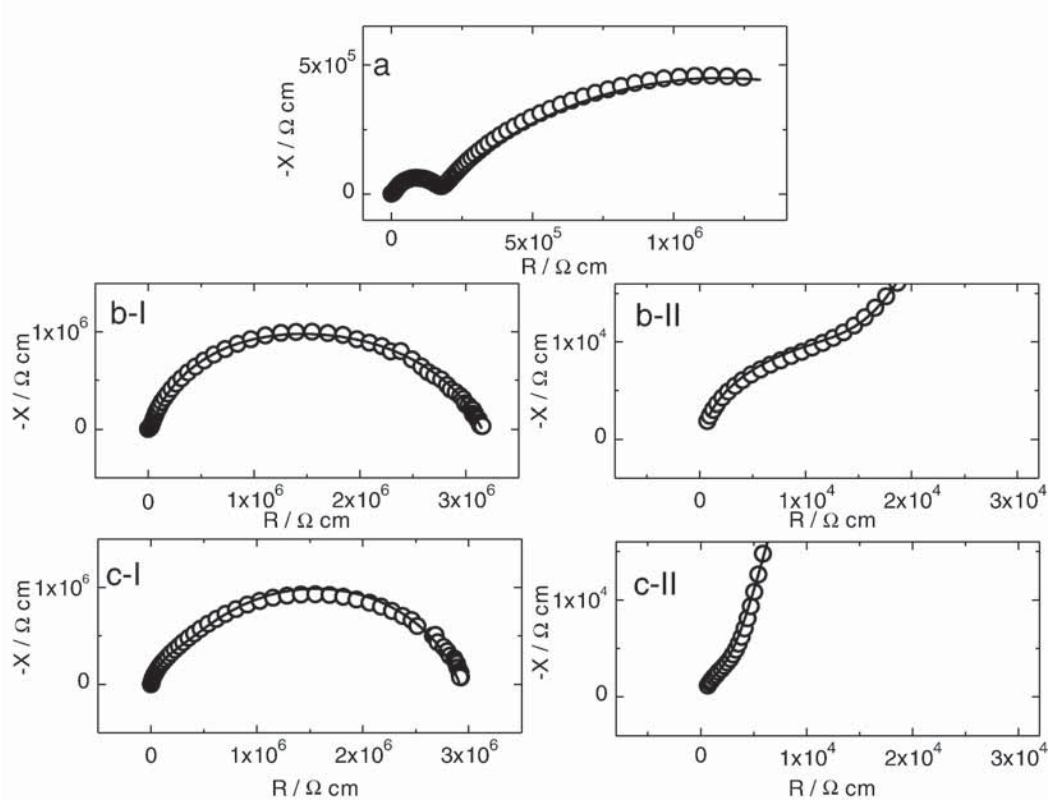

Fig. 3. Nyquist plots of a) BZY10-SPS under wet H_2 at 250 °C where the grain interior, grain boundary and electrode arcs are visible, b-I) BZY10-SPS under wet O_2 at 250 °C where the grain interior and grain boundary arcs are visible, b-II) high frequency range of b-I which magnifies the grain interior arc, c-I) BZY10-HP under wet O_2 at 350 °C showing a distorted grain boundary arc, and c-II) high frequency range of c-I magnifying the grain interior arc.

spectrum. Based on a simple fractal model, Branković et al. [34] showed that the existence of an inhomogeneous distribution of charge carriers in the vicinity of the grain boundary core results in a similarly distorted grain boundary arc. We conclude therefore that the distortion in the grain boundary arc for both the BZY10-SPS and BZY10-HP sample can originate from the distribution of impedance over the space–charge layers adjacent to a charged grain boundary core.

4.2. Yttrium distribution

Elemental distributions of Ba, Zr and Y in the grain interior and grain boundaries were investigated by TEM EDS spot analysis with a spot size of ~5 nm. In both samples the concentration of yttrium was higher in the grain boundaries compared to the grain interior as shown by the Y/Zr ratio reported in Table 1. A similar observation was made by Groß et al. [28] on $BaZr_{0.85}Y_{0.15}O_{2.925}$. Yttrium can segregate into the grain boundary core because of elastic strain due to the size mismatch of the cations (1.01 Å for Y^{3+} and 0.84 Å for Zr^{4+}). This would counteract the positive charge of the core. However, an increase in yttrium concentration at the grain boundary region is also in agreement with the overall picture that defects with effectively negative charge such as Y'_{Zr} accumulate in the space–charge layers to compensate the effectively positive core. This would counteract the depletion of protons. Here, we recall that the cation distribution

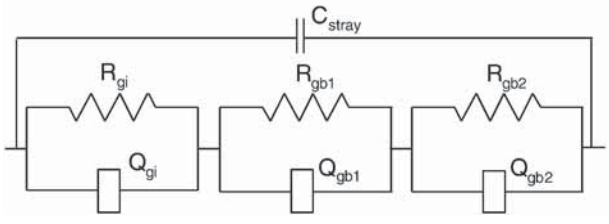

Fig. 4. Schematic equivalent circuit used for deconvoluting the impedance spectra. See text for details.

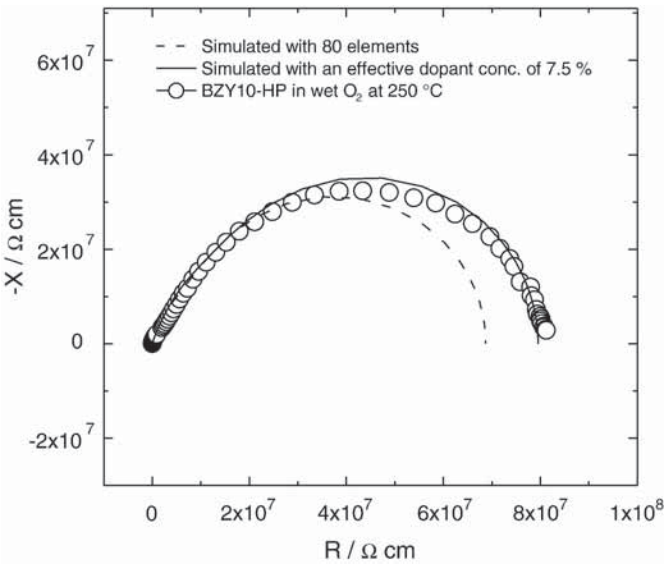

Fig. 5. Nyquist plot consisting of two simulated impedance spectra, with effective dopant concentrations of 10 and 7.5% and a spectrum obtained from the BZY10-HP sample at 250 °C in wet O_2. Only the grain boundary response is shown. See text for details.

Table 1
Y/Zr ratios obtained from EDS spot analyses of the grain interior and grain boundaries.

	Grain interior (Y/Zr)	Grain boundary (Y/Zr)
BZY10-HP	0.10 ± 0.01	0.14 ± 0.02
BZY10-SPS	0.07 ± 0.01	0.13 ± 0.04

profile is "frozen-in" below 1000 °C, the profile has most probably been set during sintering. Based on accumulation of acceptor dopants both in the grain boundary core and space–charge layers, it becomes apparent that one may decrease the grain boundary resistance by increasing the dopant concentration. This has been shown for CeO_2 doped with various amounts of Y_2O_3 [20]. Indications of similar behaviour for Y-doped $BaZrO_3$ will be discussed later.

4.3. p_{O_2} dependencies

Fig. 6 shows the P_{O_2}-dependencies of the specific grain interior and grain boundary conductivity BZY10-SPS at 250 °C. Under oxidizing conditions protons dominate the conductivity, and the conductivity is thus independent of p_{O_2}. Under reducing conditions, the grain interior conductivity is independent of p_{O_2}, reflecting dominating ionic conduction, whereas the grain boundary conductivity increases weakly with decreasing p_{O_2}, indicating mixed ionic and n-type electronic conduction. The difference between grain interior and grain boundary conductivity under reducing conditions may be attributed to an accumulation of electrons in the space–charge layer due to a positive grain boundary core. A similar accumulation of electrons under reducing conditions has been demonstrated for acceptor doped CeO_2 [20].

4.4. Schottky barrier heights

Calculated Schottky barrier heights are given in Table 2. The observed difference in Schottky barrier height under wet conditions of ~0.1 V between BZY10-HP and BZY10-SPS reflects most probably the sensitivity of sample preparation of BZY which has been shown to give

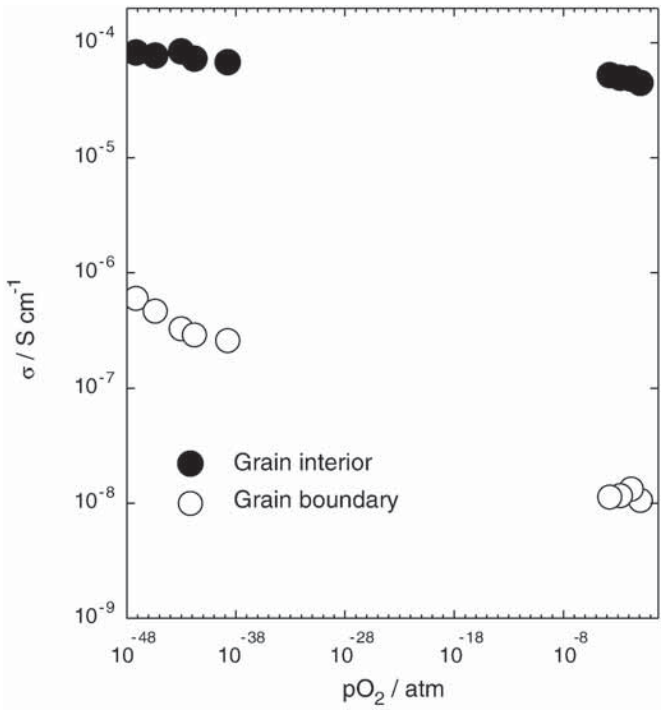

Fig. 6. P_{O_2}-dependency of specific conductivities for BZY10-SPS under wet conditions at 250 °C.

Table 2
Schottky barrier heights and activation energies under wet ($P_{H_2O} = 0.025$ atm) and dry ($P_{H_2O} \approx 3 \cdot 10^{-5}$ atm) oxidizing conditions. Values at 300, 250 and 200 °C based on conductivities calculated from Eq. (11). Values in parentheses indicate statistical errors. The temperature interval from which the activation energy is calculated is given in parenthesis. All Schottky barrier heights for wet conditions are calculated using the model derived here for proton conductors, while the ones for dry conditions (*) are calculated using a model for oxygen ion conduction via divalent oxygen vacancies.

		$\Delta\varphi(0)$ (V)			Activation energy, E_A, (kJ·mol^{-1})	
		300 °C	250 °C	200 °C	Grain interior	Grain boundaries
BZY10-HP	Wet O_2	0.62	0.63	0.63	47 (±1) (550–200 °C)	110 (±1) (350–200 °C)
BZY10-SPS	Wet O_2	0.51	0.48	0.51	45 (±1) (500–150 °C)	81 (±5) (350–150 °C)
	Dry O_2	0.22*	0.21*	0.22*	72 (±3) (500–150 °C)	97 (±2) (300–150 °C)
BZY10 Duval et al. [35]	Wet O_2	0.46	0.47	0.47		
BZY20 Babilo et al. [31]	Wet O_2	0.44	0.42	0.41		

variations in the electrical properties (see e.g. overview by Babilo et al. [31]).

If the grain boundary core and the dopant concentration are constant and we assume a Mott–Schottky approximation, the Schottky barrier height, $\Delta\varphi(0)$ and the space–charge layer width, λ^*, should be independent of type of charge carrier. If we furthermore assume that the grain boundary core is unchanged going from wet to dry conditions, $\Delta\varphi(0)$ should be constant as a function of water vapour pressure. In Table 2 we see however that $\Delta\varphi(0)$ comes out smaller under dry compared to wet conditions (the analysis assumes that oxygen vacancies dominate under dry and protons under wet conditions). If oxygen vacancies do not dominate, and instead protons or electron holes dominate under dry conditions, the calculated $\Delta\varphi(0)$ would be 0.41 V, closer to, but still lower than that calculated under wet conditions, 0.50 V. A difference in $\Delta\varphi_{wet}(0)$ and $\Delta\varphi_{dry}(0)$ may therefore instead originate from a change in the core charge. The following possible hydration reaction of the core is suggested (in Kröger–Vink notation):

$$H_2O(g) + V^{\bullet\bullet}_{O,gi} + 2O^{x}_{O,core} = O^{x}_{O,gi} + 2OH^{\bullet}_{O,core}. \quad (15)$$

If we assume that oxygen vacancies are stabilised in the grain boundary core in order to decrease its mismatch energy, these vacancies will not be easily filled, and grain interior vacancies are then selectively filled during hydration. For the protons from the dissolved water it is, however, probably favourable to settle in the grain boundary core where they can terminate mismatched oxygen ions and further contribute to a decrease of the mismatch energy. Such a grain boundary core hydration would explain the observed difference in Schottky barrier height under wet and dry conditions.

Table 2 shows estimated Schottky barrier heights based on specific grain interior and grain boundary conductivities reported by Duval et al. [35] on a BZY10 sample and by Babilo et al. [31] on a 20 mol% Y-doped $BaZrO_3$ (BZY20). The latter conductivity data are re-plotted in Fig. 8. The scattering of the Schottky barrier height for the BZY10 samples reflects the variations of conductivity reported in literature due to differences in preparation. The lower Schottky barrier height of the BZY20 sample indicates a decreasing height with increasing dopant concentration, which is in accordance with results obtained for Y_2O_3-doped CeO_2. [20].

Our values for the Schottky barrier height (Table 2) are comparable with values reported for 1 mol% Y_2O_3-doped CeO_2 (~0.5 V) [20] and higher than those reported for 8 mol% Y_2O_3-substituted ZrO_2 [1] (~0.3 V). The relatively large value of the Schottky barrier height is

reflected in the dominating grain boundary resistance of Y-doped $BaZrO_3$.

A Schottky barrier height cannot be calculated from the total grain interior and grain boundary conductivities when different species dominate the grain interior and grain boundary conductivity (knowledge of the partial conductivities would be needed). This is the case for BZY10-SPS under reducing conditions, where it has an additional electronic contribution besides the protonic grain boundary conduction. It is, however interesting to point out the difference between the grain interior and grain boundary conductivity under reducing and oxidizing conditions in Fig. 4. Under oxidizing conditions, the grain boundary conductivity is approximately 4 orders of magnitude below the grain interior conductivity, while the difference is only 2 orders of magnitude under reducing conditions. This difference may reflect an increased concentration of electrons in the space–charge layer as part of the accumulation of negative defects, and therefore indeed supports the existence of space–charge layers.

4.5. Defect concentration profile in the space–charge layer

In the temperature interval measured it is reasonable to assume that the acceptor dopant is "frozen-in". If we, to a first approximation, assume that the yttrium concentration is uniformly distributed throughout the sample, the Mott–Schottky approach can, as discussed above, be applied. Fig. 7 shows normalized defect concentration profiles estimated at 200, 250 and 300 °C in wet oxygen based on conductivity data of BZY10-SPS. The data for BZY10-HP give analogous profiles (not included). The calculated space–charge layer widths for the two samples are 4.3 nm for BZY10-SPS and 4.0 nm for BZY10-HP, i.e., equal within experimental uncertainty. The normalized concentration of protons in the space–charge layer decreases with decreasing temperature (Eq. (10)), while the space–charge layer width is independent of temperature (Eq. (9)) taking into account the experimentally observed temperature independent Schottky barrier height. From this, one may conclude that it is only the temperature dependency of the Debye length that determines the change in the concentration profile with temperature. The Debye length has a $T^{1/2}$ dependence (Eq. (8)) and is furthermore dependent on the concentration of charge carriers, c_Y, which is, however, assumed independent of temperature.

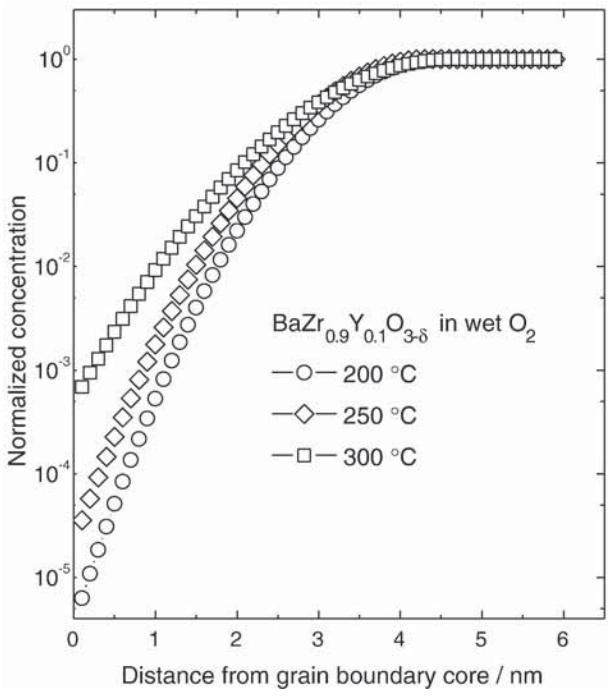

Fig. 7. Normalized concentration of protons in the space–charge layer relative to the concentration in the grain interior calculated on basis of data from BZY10-SPS at 200, 250 and 300 °C.

4.6. Activation energies

Activation energies of specific conductivities are given in Table 2. The activation energies for grain interior under wet conditions (i.e. for the proton mobility) are 47 (±1) kJ mol^{-1} for BZY10-HP and 45 (±1) kJ mol^{-1} for BZY10-SPS and the grain boundary activation energy for BZY10-SPS is 81 (±5) kJ mol^{-1}, and these are comparable with the grain interior activation energy, 45 (±1) kJ mol^{-1}, and the grain boundary activation energy, ~68 kJ mol^{-1}, reported by Bohn and Schober [5] in the same temperature interval. The higher grain boundary activation energy for BZY10-HP, 110 (±1) kJ mol^{-1} is reflected in the higher Schottky barrier height calculated for this sample, as mentioned above.

4.7. Implications for overall conductivity

Available literature on substituted $BaZrO_3$ materials tends to report the total conductivity without delineation into grain interior and grain boundary conductivities (see e.g. [36–38]). Few have reported grain boundary specific conductivities or resistivities (see e.g. [31,35]) which are needed to compare grain boundary properties. Fig. 8 shows collected literature results on grain interior and specific grain boundary conductivities of acceptor doped $BaZrO_3$ compared with the samples measured in this work. The grain interior conductivities of BZY10 samples are in the same range, and deviations can probably be ascribed to the different sintering routes which lead to structural deviations as discussed by Azad et al. [39]. A higher

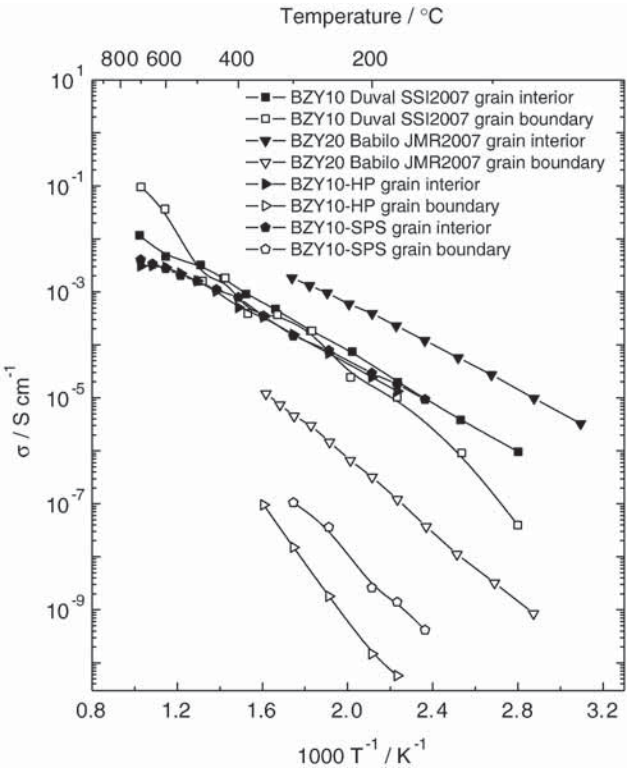

Fig. 8. Specific grain interior and grain boundary conductivity vs. inverse temperature for BZY10-HP and BZY10-SPS compared with literature data. The BZY10 sample measured by Duval et al. [35] was annealed to ~2200 °C which significantly decreased the grain boundary resistance. The BZY20 data from Babilo et al. [31] are included to indirectly illustrate how the Schottky barrier height decreases with increasing dopant concentration.

dopant concentration of BZY20 increases the concentration of protons and thereby the grain interior conductivity as seen from Babilo et al. [31]. Both BZY10-HP and BZY10-SPS show the typical low grain boundary conductivity observed in $BaZrO_3$ compounds. The differences between them may reflect the different sintering techniques or implications of the bimodal grain size distribution for BZY10-SPS. The exceptionally high grain boundary conductivities from the work of Duval et al. [35] resulted from annealing at very high temperatures. It was suggested that changes in the composition or structure of the boundary could change the nature of a space–charge region and, in turn, the concentration and conductivity of protons across the grain boundaries. We speculate further whether the grain boundary core potential was levelled out compared to the grain interior potential due to cation (including dopant) redistribution at the high temperatures. These results, together with the results from the present work, are strong indications that a charged grain boundary core and space–charge layers exist and rule the grain boundary resistances in $BaZrO_3$ ceramics.

5. Summary and conclusions

(1) Impedance spectroscopy was used to investigate the grain boundary electrical properties of 10% Y-doped $BaZrO_3$. Spark plasma sintering (BZY10-SPS) and hot pressing (BZY10-HP) were applied to achieve reasonable densities without loss of barium. Specific grain boundary conductivities were obtained using the brick layer model.

(2) p_{O_2}-dependencies for the BZY10-SPS sample were indicative of proton conduction in the grain interior and a reduced proton conductivity across the grain boundaries, while under reducing conditions the grain boundaries showed an additional n-type contribution. All this supports the prevailing view of positively charged grain boundary cores with depletion of positive defects and accumulation of negative negatively charge defects in the adjacent space–charge layers.

(3) Schottky barrier heights were calculated from specific proton conductivities. By way of example, the Schottky barrier height at 250 °C was 0.5–0.6 V.

(4) With the obtained Schottky barrier heights, space–charge defect profiles were calculated. The model implies that the concentration of protons in the space–charge layer decreases while the space–charge layer width is constant with decreasing temperature. The space–charge layer width was around 4 nm in both BZY10-SPS and BZY10-HP. A difference in Schottky barrier height under wet and dry conditions was proposed due to a hydration process where the grain boundary core oxide ions were preferentially protonated but while grain interior oxygen vacancies were preferentially consumed.

(5) A simulated impedance spectrum based on the space–charge layer defect concentration profile gave a distortion in the grain boundary arc similar to that observed experimentally.

Acknowledgment

This work has been funded by the FUNMAT@UiO program for CK, and by the NANOMAT program of the Research Council of Norway (RCN, Grant No. 15851/431, "Functional oxides for energy technology (FOET)") for RH.

References

[1] X. Guo, W. Sigle, J. Fleig, J. Maier, Solid State Ionics 154–155 (2002) 555.
[2] A. Tschöpe, E. Sommer, R. Birringer, Solid State Ionics 139 (3,4) (2001) 255.
[3] X. Guo, J. Fleig, J. Maier, Journal of the Electrochemical Society 148 (9) (2001) J50.
[4] S.M. Haile, D.L. West, J. Campbell, Journal of Materials Research 13 (6) (1998) 1576.
[5] H.G. Bohn, T. Schober, Journal of the American Ceramic Society 83 (4) (2000) 768.
[6] K.D. Kreuer, Solid State Ionics 125 (1–4) (1999) 285.
[7] R. Haugsrud, T. Norby, Nature Materials 5 (3) (2006) 193.
[8] T. Schober, H.G. Bohn, Solid State Ionics 127 (3,4) (2000) 351.
[9] M. Aoki, Y.-M. Chiang, I. Kosacki, L.J.-R. Lee, H. Tuller, Y. Liu, Journal of the American Ceramic Society 79 (5) (1996) 1169.
[10] S.P.S. Badwal, Solid State Ionics 76 (1,2) (1995) 67.
[11] M. Gödickemeier, B. Michel, A. Orliukas, P. Bohac, K. Sasaki, L. Gauckler, H. Heinrich, P. Schwander, G. Kostorz, Journal of Materials Research 9 (5) (1994) 1228.
[12] X. Guo, R. Waser, Progress in Materials Science 51 (2) (2006) 151.
[13] T.S. Zhang, J. Ma, Y.Z. Chen, L.H. Luo, L.B. Kong, S.H. Chan, Solid State Ionics 177 (13–14) (2006) 1227.
[14] S. Kim, J. Maier, Journal of the Electrochemical Society 149 (10) (2002) J73.
[15] H.J. Park, S. Kim, Journal of Physical Chemistry C 111 (40) (2007) 14903.
[16] Y. Ikuhara, P. Thavorniti, T. Sakuma, Acta Materialia 45 (12) (1997) 5275.
[17] F. Iguchi, N. Sata, T. Tsurui, H. Yugami, Solid State Ionics 178 (7–10) (2007) 691.
[18] F. Iguchi, T. Tsurui, N. Sata, Y. Nagao, H. Yugami, Solid State Ionics 180 (6–8) (2009) 563.
[19] X. Guo, J. Maier, Journal of the Electrochemical Society 148 (3) (2001) E121.
[20] X. Guo, W. Sigle, J. Maier, Journal of the American Ceramic Society 86 (1) (2003) 77.
[21] J. Fleig, J. Maier, Journal of the European Ceramic Society 19 (6–7) (1999) 693.
[22] J. Fleig, Solid State Ionics 131 (1,2) (2000) 117.
[23] X. Guo, Y. Ding, Journal of the Electrochemical Society 151 (1) (2004) J1.
[24] X. Guo, R. Waser, Solid State Ionics 173 (1–4) (2004) 63.
[25] S. Kim, J. Fleig, J. Maier, Physical Chemistry Chemical Physics 5 (11) (2003) 2268.
[26] A. Tschöpe, Solid State Ionics 139 (3,4) (2001) 267.
[27] S.L. Hwang, I.W. Chen, Journal of the American Ceramic Society 73 (1990) 3269.
[28] B. Groß, C. Beck, F. Meyer, T. Krajewski, R. Hempelmann, H. Altgeld, Solid State Ionics 145 (1–4) (2001) 325.
[29] P.I. Dahl, *PhD thesis* (NTNU, Trondheim, Norway 2006).
[30] B.A. Boukamp, Equivalent Circuit for Windows Ver. 1.0, 2003.
[31] P. Babilo, T. Uda, S.M. Haile, Journal of Materials Research 22 (5) (2007) 1322.
[32] J. Fleig, P. Pham, P. Sztulzaft, J. Maier, Solid State Ionics 113–115 (1998) 739.
[33] J. Fleig, Journal of Electroceramics 13 (2004) 637.
[34] G. Branković, Z. Branković, V.D. Jović, J.A. Varela, Journal of Electroceramics 7 (2001) 89.
[35] S.B.C. Duval, P. Holtappels, U.F. Vogt, E. Pomjakushina, K. Conder, U. Stimming, T. Graule, Solid State Ionics 178 (25–26) (2007) 1437.
[36] K. Nomura, H. Kageyama, Solid State Ionics 178 (7–10) (2007) 661.
[37] R.C.T. Slade, S.D. Flint, N. Singh, Solid State Ionics 82 (3,4) (1995) 135.
[38] F.M.M. Snijkers, A. Buekenhoudt, J. Cooymans, J.J. Luyten, Scripta Materialia 50 (5) (2004) 655.
[39] A.K. Azad, C. Savaniu, S. Tao, S. Duval, P. Holtappels, R.M. Ibberson, J.T.S. Irvine, Journal of Materials Chemistry 18 (29) (2008) 3414.